Polar stratospheric nitric acid depletion surveyed from a decadal dataset of IASI total columns

Gaetane Ronsmans[1], Catherine Wespes[1,*], Lieven Clarisse[1], Susan Solomon[2], Daniel Hurtmans[1], Cathy Clerbaux[1,3], and Pierre-François Coheur[1]

[1]Université libre de Bruxelles (ULB), Spectroscopy, Quantum Chemistry and Atmospheric Remote Sensing (SQUARES), Brussels, Belgium
[2]Department of Earth, Atmospheric and Planetary Sciences, Massachusetts Institute of Technology, Cambridge, Massachusetts, USA
[3]LATMOS/IPSL, Sorbonne Université, UVSQ, CNRS, Paris, France

Correspondence: Catherine Wespes (cwespes@ulb.ac.be)

Abstract

In this paper, we exploit the first 10-year data-record (2008-2017) of nitric acid (HNO_3) total columns measured by the IASI-A/Metop infrared sounder, characterized by an exceptional daily sampling and a good vertical sensitivity in the mid-stratosphere (around 50 hPa), to monitor the causal relationship between the temperature decrease and the observed HNO_3 loss that occurs each year in the Antarctic stratosphere during the polar night. Since the HNO_3 depletion results from the formation of polar stratospheric clouds (PSCs) which trigger the development of the ozone (O_3) hole, its continuous monitoring is of high importance. We verify here, from the 10-year time evolution of the pair HNO3-temperature (taken from reanalysis at 50 hPa), the recurrence of specific regimes in the cycle of IASI HNO_3 and identify, for each year, the day and the 50 hPa temperature ("drop temperature") corresponding to the onset of strong HNO_3 depletion in the Antarctic winter. Although the measured HNO_3 total column does not allow differentiating the uptake of HNO_3 by different types of PSC particles along the vertical profile, an average drop temperature of ~194.2 ± 3.8 K, consistent with the nitric acid trihydrate (NAT) formation temperature (close to 195 K at 50 hPa), is found in the region of potential vorticity lower than -10×10^{-5} $K.m^2.kg^{-1}.s^{-1}$. The spatial distribution and inter-annual variability of the drop temperature are investigated and discussed in the context of previous PSCs studies. This paper highlights the capability of the IASI sounder to monitor the long-term evolution of the polar stratospheric composition and processes involved in the depletion of stratospheric O_3.

1 Introduction

The cold and isolated air masses found within the polar vortex during winter are associated with a strong denitrification of the stratosphere due to the formation of PSCs (composed of HNO_3, sulphuric acid (H_2SO_4) and water ice (H_2O)) (Peter, 1997; Voigt et al., 2000; von König, 2002; Schreiner et al., 2003; Peter and Grooß, 2012). These clouds strongly affect the polar chemistry by (1) acting as surfaces for the heterogeneous activation of chlorine and bromine compounds, in turn leading to enhanced O3 destruction (Solomon, 1999; Wang and Michelangeli, 2006; Harris et al., 2010; Wegner et al., 2012) and by (2) removing gas-phase HNO_3 temporarily or permanently through uptake by PSCs and sedimentation of large PSC particles to lower altitudes. The denitrification of the polar stratosphere during winter delays the reformation of chlorine reservoirs and, hence, intensifies the O_3 hole (Solomon, 1999; Harris et al., 2010). The heterogeneous reaction rates on PSCs surface and the uptake of HNO_3 strongly depend on the temperature and on the PSCs particle type. The PSCs are classified into three 3different types based on their composition and optical properties: type Ia solid nitric acid trihydrate -

NAT (HNO_3.$(H_2O)_3$), type Ib liquid supercooled ternary solution - STS ($HNO_3/H_2SO_4/H_2O$ with variable composition) and type II, crystalline water-ice particles (likely composed of a combination of different chemical phases) (Toon et al., 1986; Koop et al., 2000; Voigt et al., 2000; Lowe and MacKenzie, 2008). In the stratosphere, they mostly consist of mixtures of liquid/solid STS/NAT particles in varying number densities, with HNO_3 being the major constituent of these particles. The large-size NAT particles of low number density are the principal cause of sedimentation (Lambert et al., 2012; Pitts et al., 2013; Molleker et al., 2014; Lambert et al., 2016). The formation temperature of STS (T_{STS}) and the thermodynamic equilibrium temperatures of NAT (T_{NAT}) and ice (T_{ice}), have been determined, respectively, as: ~192 K (Carslaw et al., 1995), ~195.7 K (Hanson and Mauersberger, 1988) and ~188 K (Murphy and Koop, 2005) for typical 50 hPa atmospheric conditions (5 ppmv H_2O and 10 ppbv HNO_3). While the NAT nucleation was thought to require temperatures below T_{ice} and pre-existing ice particles, recent observational and modelling studies have shown that HNO_3 starts to condense in early PSC season in liquid NAT mixtures well above T_{ice} (~4 K below T_{NAT} , close to T_{STS}) even after a very short temperature threshold exposure (TTE) to these temperatures but also slightly below T_{NAT} after a long TTE, whereas the NAT existence persists up to T_{NAT} (Pitts et al., 2013; Hoyle et al., 2013; Lambert et al., 2016; Pitts et al., 2018). It has been recently proposed that the higher temperature condensation results from heterogeneous nucleation of NAT on meteoritic dust in liquid aerosol (Hoyle et al., 2013; Grooß et al., 2014; James et al., 2018). Further cooling below T_{STS} and T_{ice} leads to nucleation of liquid STS, of solid NAT onto ice and of ice particles mainly from STS (type II PSCs) (Lowe and MacKenzie, 2008). The formation of NAT and ice has also been shown to be triggered by stratospheric mountain-waves (Carslaw et al., 1998; Hoffmann et al., 2017). Although the formation mechanisms and composition of STS droplets in stratospheric conditions are well described (Toon et al., 1986; Carslaw et al., 1995; Lowe and MacKenzie, 2008), the NAT and ice nucleation processes still require further investigation. This could be important as the chemistry-climate models (CCMs) generally oversimplify the heterogeneous nucleation schemes for the PSCs formation (Zhu et al., 2015; Spang et al., 2018; Snels et al., 2019) preventing an accurate estimation of O_3 levels. The influence of HNO_3 in modulating O_3 abundances in the stratosphere is furthermore underrepresented in CCMs (Kvissel et al., 2012).

Several satellite instruments measure stratospheric HNO_3 (e.g. MLS/UARS (Santee et al., 1999), MLS/Aura (Santee et al., 2007), MIPAS/ENVISAT (Piccolo and Dudhia, 2007), ACE-FTS/SCISAT (Sheese et al., 2017) and SMR/Odin (Urban et al., 2009)). The spaceborne lidars CALIOP/CALIPSO and the infrared instrument MIPAS/Envisat) are capable to detect and classify the PSC types, and to follow their formation mechanisms (Lambert et al., 2016; Pitts et al., 2018; Spang et al., 2018) and references therein, which complements in situ measurements (Voigt et al., 2005) and ground-based lidar (Snels et al., 2019). From these available observational datasets, the HNO_3 depletion has been linked to the PSCs formation and detected below the T_{NAT} threshold (Santee et al., 1999; Urban 55 et al., 2009; Lambert et al., 2016; Ronsmans et al., 2018), but its relationship to PSCs still needs further investigation given the complexity of the nucleation mechanisms that depends on a series of parameters (e.g. atmospheric temperature, water and HNO_3 vapour pressure, time exposure to temperatures, temperature history).

In contrast to the limb satellite instruments mentioned above, the infrared nadir sounder IASI offers a dense spatial sampling of the entire globe, twice a day (Section 2). While it cannot provide a vertical profile of HNO_3 similar to the limb sounders, IASI provides reliable total column measurements of HNO_3 characterized by a maximum sensitivity in the low-middle stratosphere around 50 hPa (20 km) during the dark Antarctic winter (Ronsmans et al., 2016, 2018) where the PSCs cloud form (Voigt et al., 2005; Lambert et al., 2012; Spang et al., 2016, 2018). This study aims to explore the 10-years continuous HNO_3 measurements from IASI for providing a long-term global picture of depletion and of its dependence to temperatures during polar winter (Section 3). The temperature corresponding to the onset of the strong depletion in HNO_3 records (here referred to as 'drop temperature') is identified in Section 4 for each observed year and discussed in the context of previous studies.

2 Data

The HNO_3 data used in the present study are obtained from measurements of the Infrared Atmospheric Sounding Interferometer (IASI) embarked on the Metop-A satellite. IASI measures the Earth's and atmosphere's radiation in the thermal infrared spectral range (645 - 2760 cm^{-1}), with a 0.5 cm^{-1} apodized resolution and a low radiometric noise (Clerbaux et al., 2009; Hilton et al., 2012). Thanks to its polar sun-synchronous orbit with more than 14 orbits a day and a field of view of four simultaneous footprints of 12 km at nadir, IASI provides global coverage twice a day (9.30 AM and PM mean local solar time). That extensive spatial and temporal sampling in the polar regions is key to this study.

The HNO_3 vertical profiles are retrieved on a uniform vertical 1 km grid of 41 layers (from the surface to 40 km with an extra layer above to 60 km) in near-real-time by the Fast Optimal Retrieval on Layers for IASI (FORLI) software, using the optimal estimation method (Rodgers, 2000). Detailed information on the FORLI algorithm and retrieval parameters specific to HNO_3 can be found in previous papers (Hurtmans et al., 2012; Ronsmans et al., 2016). For this study, only the total columns (v20151001) are used, considering (1) the low vertical resolution of IASI with only one independent piece of information, (2) the limited sensitivity of IASI to tropospheric HNO_3, (3) the dominant contribution of the stratosphere to the HNO_3 total column and (4) the largest sensitivity of IASI in the region of interest, i.e. in the low and mid-stratosphere (from ~70 to ~30 hPa), where the HNO_3 abundance is the highest (Ronsmans et al., 2016). The total columns are associated with a total retrieval error ranging from around 3% at mid- and polar latitudes to 25% above cold Antarctic surface during winter (due to a weaker sensitivity above very cold surface with a DOFS of 0.95 and to an poor knowledge of the seasonally and wavenumber-dependent emissivity above ice surfaces which induces larger forward model errors), and a low bias (lower than 12%) in polar regions over the altitude range where the IASI sensitivity is the largest, when compared to ground-based FTIR measurements (see Hurtmans et al., 2012 and Ronsmans et al., 2016 for more details). In order to expand on the comparisons against FTIR measurements which is impossible during the polar night, Figure 1 (top panel) presents the time series of daily IASI total HNO_3 columns co-located with MLS VMR measurements within 2.5×2.5 grid boxes at three pressure levels (at 30, 50 and 70 hPa), averaged in the 70° - 90° S equivalent latitude band. Similar variations in HNO_3 are captured by the two instruments with an excellent agreement for the timing of the strong HNO_3 depletion within the inner vortex core. IASI HNO_3 variations generally match well those of MLS HNO_3 in each latitude band (see Figure 1 bottom panel for the 50° - 70° S equivalent latitude band; the other bands are not shown here).

Quality flags similar to those developed for O_3 in previous IASI studies (Wespes et al., 2017) were applied a posteriori to exclude data (i) with a corresponding poor spectral fit (e.g. based on quality flags rejecting biased or sloped residuals, fits with maximum number of iteration exceeded), (ii) with less reliability (e.g. based on quality flags rejecting suspect averaging kernels, data with less sensitivity characterized by a DOFS lower than 0.9) or (iii) with tropospheric cloud contamination (defined by a fractional cloud cover ≥ 25 %). Note that the HNO_3 total column distributions illustrated in sections below use the median as a statistical average since it is more robust against the outliers than the mean.

Temperature and potential vorticity (PV) fields are taken from the ECMWF ERA Interim Reanalysis dataset, respectively at 50 hPa and at the potential temperature of 530 K (corresponding to ~20 km altitude where the IASI sensitivity to HNO_3 is the highest during the Southern Hemisphere (S.H.) winter (Ronsmans et al., 2016). Because the HNO_3 uptake by PSCs starts a few degrees or slightly below T_{NAT}

(~195.7 K at 50 hPa (Hanson and Mauersberger, 1988)) depending on the meteorological conditions (Pitts et al., 2013; Hoyle et al., 2013; Lambert et al., 2016; Pitts et al., 2018), a threshold temperature of 195 K is considered in the sections below to identify the PSCs-containing regions. The potential vorticity is used to delimit dynamically consistent areas in the polar regions. In what follows, we use either the equivalent latitudes ("eqlat", calculated from PV fields at 530 K) or the PV values to characterize the relationship between HNO_3 and temperatures in the cold polar regions. Uncertainties in ERA-Interim temperatures will also be discussed below.

3 Annual cycle of HNO_3 vs temperatures

Figure 2a shows the yearly HNO_3 cycle (solid lines, left axis) in the southernmost equivalent latitudes (70° - 90° S), as measured by IASI over the whole period of measurements (2008–2017). The total HNO_3 variability in such equivalent latitudes has already been discussed in a previous IASI study (Ronsmans et al., 2018) where the contribution of the PSCs into the HNO_3 variations was highlighted. The temperature time series, taken at 50 hPa, is here represented as well (dashed lines, right axis). From this figure, different regimes of HNO_3 total columns *vs* temperature can be observed throughout the year and from one year to another. In particular, we define here three main regimes (R1, R2 and R3) along the HNO_3/temperature cycle. The full cycle and the main regimes in the 70° - 90° S eqlat region are further represented in Fig. 2b that shows a histogram of the HNO_3 total columns as a function of temperature for the year 2011. Similar histograms are observed for the ten years of IASI measurements (not shown). The red horizontal and vertical lines in Fig. 2a and Fig. 2b, respectively, represent the 195 K threshold temperature used to identify the onset of HNO_3 uptake by PSCs (see Section 2). The three identified regimes correspond to:

- R1 is defined by the maxima in the total HNO_3 abundances covering the months of April and May (~3×10^{16} molec.cm^{-2}, R1 in Figures 2a and b), when the 50 hPa temperature strongly decreases (from ~220 to ~195 K). These high HNO_3 levels result from low sunlight, preventing photodissociation, along with the heterogeneous hydrolysis of N_2O_5 to HNO_3 during autumn before the formation of polar stratospheric clouds (Keys et al., 1993; Santee et al., 1999; Urban et al., 2009; de Zafra and Smyshlyaev, 2001). This period also corresponds to the onset of the deployment of the southern polar vortex which is characterized by strong diabatic descent with weak latitudinal mixing across its boundary, isolating polar HNO_3-rich air from lower latitudinal airmasses.

- R2 which extends from June to October is characterized by the onset of the strong decrease in HNO_3 total columns at the beginning of June, when the temperatures fall below 195 K, followed by a plateau of total HNO_3 minima. In this regime, the HNO_3 total columns average below 2×10^{16} molec.cm^{-2} and the 50 hPa temperatures range mostly between 180 and 190 K.

- R3 starts in October when sunlight returns and the 50 hPa temperatures rise above 195 K. Despite the stratospheric warming with 50 hPa temperatures up to 240 K in summer, the HNO_3 total columns stagnate at the R2 plateau levels (around 1.5×10^{16} molec.cm^{-2}). This regime likely reflects the photolysis of NO_3 and HNO_3 itself (Ronsmans et al., 2018) as well as the permanent denitrification of the mid-stratosphere, caused by the PSCs sedimentation. The likely renitrification of the lowermost stratosphere (Braun et al., 2019; Lambert et al., 2012) where the HNO_3 concentrations and the IASI sensitivity to HNO_3 are lower (Ronsmans et al., 2016) cannot be inferred from the IASI measurements.The plateau lasts until approximately February, where HNO_3 total column slowly starts increasing, reaching the April-May maximum in R1.

As illustrated in Fig. 2a, the three regimes are observed each year with, however, some interannual variations. For instance, the sudden stratospheric warming (SSW) that occurs in 2010 (see the temperature time series at 20 hPa for the year 2010; green dotted line) yielded higher HNO_3 total columns (see green solid line in July and August) (de Laat and van Weele, 2011; Klekociuk et al., 2011; WMO, 2014; Ronsmans et al., 2018).

Figure 2c shows the evolution of the relationship between the daily averaged HNO_3 (calculated from a 7-day moving average) with the highest occurrence (in bins of 0.1×10^{16} molec.cm^{-2} and of 2K) and the 50 hPa temperature, over the 10 years of IASI. The red vertical line represents the 195 K threshold temperature. Figure 2c clearly illustrates the slow increase in HNO_3 columns as the temperatures decrease (February to May, i.e. R3 to R1), the strong and rapid HNO_3 depletion occurring in June (R2), the plateau of low HNO_3 abundances in winter and spring (from August to November; R2 to R3). Figure 2c also highlights the interannual variability in total HNO_3, which is found to be the largest in R3, and shows a strong consistency in the onset of the depletion between each year (beginning of June when the temperatures fall below 195 K as indicated by the red vertical line). Given the span of PSCs formation over a large range of altitudes (typically between 10 and 30 km) (Höpfner et al., 150 2006, 2009; Spang et al., 2018; Pitts et al., 2018) and that of maximum IASI sensitivity to HNO_3 around 50 hPa (Hurtmans et al., 2012; Ronsmans et al., 2016), the temperatures at two other pressure levels, namely 70 and 30 hPa (i.e. ~15 and ~25 km), have also been tested to investigate the relationship between HNO_3 and temperature in the low and mid-stratosphere. The results (not shown here) exhibit a similar HNO_3-temperature behavior at the different levels with, as expected, lower and larger temperatures in R2, respectively, at 30 hPa (down to ~180 K) and at 70 hPa (down to ~185 K), but still below the NAT formation threshold at these pressure levels (T_{NAT} ~193 K at 30 hPa and ~197 K at 70 hPa) (Lambert et al., 2016). Therefore, the altitude range of maximum IASI sensitivity to HNO_3 (see Section 2) is characterized by temperatures that are below the NAT formation threshold at these pressure levels, enabling the PSCs formation and the denitrification process. Furthermore, the consistency between the 195 K threshold temperature taken at 50 hPa and the onset of the strong total HNO_3 depletion seen in IASI data (see Fig. 2a and Fig. 2c) is in agreement with the largest NAT area that starts to develop in June around 20 km (Spang et al., 2018), which justifies the use of the 195 K temperature at that single representative level in this study.

4 Onset of HNO_3 depletion and drop temperature detection

To identify the spatial and temporal variability of the onset of the depletion phase, the daily time evolution of HNO_3 during the first 10 years of IASI measurements and the temperatures at 50 hPa are explored. In particular, the second derivative of HNO_3 total column with respect to time is calculated to detect the strongest rate of decrease seen in the HNO_3 time series and to identify its associated day and 50 hPa temperature.

4.1 HNO_3 vs temperature time series

Figure 3 shows the time series of the second derivative of HNO_3 total column with respect to time (blue) and of the temperature (red) averaged in the areas of potential vorticity smaller than -10×10^{-5} K.m^2.kg^{-1}.s^{-1} to encompass the regions inside the inner polar vortex where the temperatures are the coldest and the total HNO_3 depletion occurs (Ronsmans et al., 2018). The use of that PV threshold value explains the gaps in the time series during the summer when the PV does not reach such low levels, while the time series averaged in the 70°- 90° S Eqlat band (dashed blue for the second derivative of HNO_3 and grey for the temperature) covers the full year. Note that the HNO_3 time series has been smoothed with a simple spline data interpolation function to avoid gaps in order to calculate the second derivative of

HNO_3 total column with respect to time as the daily second-difference HNO_3 total column. The horizontal red line shows the 195 K threshold.

As already illustrated in Fig. 2a and Fig. 2c, the strongest rate of HNO_3 depletion (i.e. the second derivative minimum) is found around the 195 K threshold temperature, within some days (4 to 23 days) after total HNO_3 reaches its maximum, i.e. typically between the 11th of May (2013) and the 8th of June (2009). The 50 hPa drop temperatures are detected between 189.2 K and 202.8 K, with an average of 194.2 ± 3.8 K (1σ standard deviation) over the ten years. Knowing that T_{NAT} can be higher or lower depending on the atmospheric conditions and that NAT starts to nucleate from_2–4 K below T_{NAT} (Pitts et al., 2011; Hoyle et al., 2013; Lambert et al., 2016), the results here demonstrate the consistency between the 50 hPa drop temperature, i.e. the temperature associated with the strongest HNO_3 depletion detected from IASI, and the NAT formation temperature in the mid-stratosphere at polar latitudes. It further justifies the use of the single 50 hPa level for characterizing and investigating the onset of HNO_3 depletion from IASI. Nevertheless, given the range of maximum IASI sensitivity to HNO_3 around 50 hPa, typically between 70 and 30 hPa (Ronsmans et al., 2016), the drop temperatures are also calculated at these two other pressure levels (not shown here) to estimate the uncertainty of the calculated drop temperature defined in this study at 50 hPa. The 30 hPa and 70 hPa drop temperatures range respectively over 185.7 K –194.9 K and over 194.8 K – 203.7 K, with an average of 192.0 ± 2.9 K and 198.0 ± 3.2 K (1σ standard deviation) over the ten years of IASI. The average values at 30 hPa and 70 hPa fall within the 1σ standard deviation associated with the average drop temperature at 50 hPa. It is also worth noting the agreement between the drop temperatures and the NAT formation threshold at these two pressure levels (T_{NAT} ~ 193 K at 30 hPa and ~197 K at 70 hPa) (Lambert et al., 2016).

Figures 4a and b show the zonal distribution of HNO_3 total columns and of the temperature at 50 hPa, respectively, spanning 55° - 90° S over the whole IASI period, with, superimposed, three isocontour levels of potential vorticity (-10, -8 and -5×10^{-5} $K.m^2.kg^{-1}.s^{-1}$ in blue, cyan and black, respectively) and one isocontour for the 50 hPa temperature. The PV isocontour of -10×10^{-5} $K.m^2.kg^{-1}.s^{-1}$ is clearly shown to separate well the region of strong depletion in total HNO_3 according to the latitude and the time. The red vertical dashed lines indicates the average date for the drop temperatures calculated in the area of PV≤ -10×10^{-5} $K.m^2.kg^{-1}.s^{-1}$ (194.2 ± 3.8 K; see Fig. 3) over the IASI period. It shows that the strongest rate in HNO_3 depletion occurs on average a few days before June. The delay of some days between the maximum in total HNO_3 and the start of the depletion (see Fig. 3) is also visible in Fig. 4a. The yearly zonally averaged time series over the ten years of IASI can be found in Fig. 5; it shows the reproducibility of the edge of the collar HNO_3 region and of the region of the strong HNO_3 depletion, respectively delimited by the PV isocontours of -5×10^{-5} $K.m^2.kg^{-1}.s^{-1}$ and of -10×10^{-5} $K.m^2.kg^{-1}.s^{-1}$ at 50 hPa, measured by IASI from year to year.

4.2 Distribution of drop temperatures

To explore the capability of IASI to monitor the onset of HNO_3 depletion at a large scale from year to year, figure 6 shows the spatial distribution of the 50 hPa drop temperatures (based on the second derivative minima of total HNO_3 averaged in 1°×1° grid cells) inside a region delimited by a PV value of -8×10^{-5} $K.m^2.kg^{-1}.s^{-1}$, for each year of the IASI period. The green contour represents the PV isocontour of -10×10^{-5} $K.m^2.kg^{-1}.s^{-1}$, averaged over the period 10 May – 15 July for each year, which delimits our region of interest. The isocontours of 195 K for the average temperatures and the minimum temperatures, as well as the isocontour of -10×10^{-5} $K.m^2.kg^{-1}.s^{-1}$ for the minimum PV encountered at 50 hPa over the 10 May to 15 July period are also represented. The calculated drop temperatures corresponding to the onset of HNO_3 depletion inside the averaged PV isocontour are found to vary between ~180 and ~210 K and the corresponding dates range between ~mid-May and mid-July (not shown here). Note that the high extremes in the drop temperature, which are found in some cases above eastern Antarctica, should be considered with caution: they correspond to specific regions above ice surface with emissivity features that are known to yield errors in the IASI retrievals (Hurtmans et al., 2012; Ronsmans et al., 2016). Indeed, bright land surface such as ice might in some cases lead to poor HNO_3 retrievals. Although wavenumber-dependent surface emissivity atlases are used in FORLI (Hurtmans et al., 2012), this parameter remains critical and causes poorer retrievals that, in some instances, pass through the series of quality filters and could affect the drop temperature calculation.

The averaged isocontour of 195 K encircles well the area of HNO_3 drop temperatures lower than 195 K (typically from ~187 K to ~195 K), which means that the bins inside that area characterize airmasses that experience the NAT threshold temperature during a long time over the 10 May – 15 July period. That area encompasses the inner vortex core (delimited by the isocontour of -10×10^{-5} $K.m^2.kg^{-1}.s^{-1}$ for the PV averaged over the 10 May – 15 July period) and show pronounced minima (lower than -0.5×10^{14} $molec.cm^{-2}.d^{-2}$) in the second derivative of the HNO_3 total column with respect to time (not shown here), which indicate a strong and rapid HNO_3 depletion. The area enclosed between the two isocontours of 195 K for the temperatures, the averaged one and the one for the minimum temperatures, show generally higher drop temperatures and weakest minima (larger than -0.5×10^{14} $molec.cm^{-2}.d^{-2}$) in the second derivative of the HNO_3 total column (not shown). That area is also enclosed by the isocontour of -10×10^{-5} $K.m^2.kg^{-1}.s^{-1}$ for the minimum PV, meaning that the bins inside correspond, at least for one day over the 10 May – 15 July period, to airmasses located at the inner edge of the vortex and characterized by temperature lower than the NAT threshold temperature. The weakest minima in the second derivative of total HNO_3 (not shown) observed in that area indicate a weak and slow HNO_3 depletion and might be explained by a short period of the NAT threshold temperature experienced at the inner edge of the vortex. It could also reflect a mixing with strong HNO_3-depleted and colder airmasses from the inner vortex core. The mixing with these already depleted airmasses could also explained the higher drop temperatures detected in those bins. These high drop temperatures are generally detected later (after the HNO_3 depletion occurs, i.e. after the 10 May – 15 July period considered here – not shown), which supports the transport, in those bins, of earlier HNO_3-depleted airmasses and the likely mixing at the edge of the vortex. Finally, these spatial variations might also partly reflect the range of maximum sensitivity of IASI to HNO_3, while biases in ECMWF reanalysis are too small for explaining the spatial variation in drop temperatures. Thanks to the assimilation of an advanced Tiros Operational Vertical Sounder (ATOVS) around 1998–2000 in reanalyses, to the better coverage of satellite instruments and to the use of global navigation satellite system (GNSS) radio occultation (RO) (Schreiner et al., 2007; Wang et al., 2007; Lambert and Santee, 2018; Lawrence et al., 2018), the uncertainties have been vastly reduced. Comparisons of the ECMWF ERA Interim dataset used in this work with the COSMIC data (Lambert and Santee, 2018) found a small warm bias, with median differences around 0.5 K, reaching 0–0.25 K in the southernmost regions of the globe at ~68–21 hPa where PSCs form.

Except above some parts of Antarctica which are prone to larger retrieval errors, the overall range in the drop 50 hPa temperature for total HNO_3 inside the isocontour for the averaged temperature of 195 K, typically extends from ~187 K to ~195 K, which falls within the range of PSCs nucleation temperature at 50 hPa: from slightly below T_{NAT} to around 3-4 K below the ice frost point - T_{ice} - depending on atmospheric conditions, on TTE and on the type of formation mechanisms (Pitts et al., 2011; Peter and Grooß, 2012; Hoyle et al., 2013). This underlines well the benefit of the excellent spatial and temporal coverage of IASI that allows capturing the rapid and critical depletion phase over a large scale.

5 Conclusions

In this paper, we have explored the added value of the dense HNO_3 total columns dataset provided by the IASI/Metop satellite over a full decade (2008–2017) for monitoring the stratospheric depletion phase that occurs each year in the S.H. and for investigating its relationship to the NAT formation temperature. To that end, we focused on and delimited the coldest polar region of the S.H. using a specific PV value at 530 K (~50 hPa, PV of -10×10^{-5} $K.m^2.kg^{-1}.s^{-1}$) and stratospheric temperatures at 50 hPa, taken from the ECMWF ERA Interim reanalysis. That single representative pressure level has been considered in this study given the maximum sensitivity of IASI to HNO_3 around that level over a range where the PSCs formation/denitrification process occur.

The annual cycle of total HNO_3, as observed from IASI, has first been characterized according to the temperature evolution. Three various regimes (R1 to R3) in the total HNO_3 - 50 hPa temperature relationship were highlighted from the time series over the S.H. polar region and described along the cycle: R1 is defined at play during April and May and characterized by a rapid decrease in 50 hPa temperatures while HNO_3 accumulates in the poles; R2, from June to September, shows the onset of the depletion when the 50 hPa temperatures fall below 195 K (considered here as the onset of PSCs nucleation phase at that level), with a strong consistency between each year; R3, defined from November until March when total HNO_3 remains at low R2 plateau levels, despite the return of sunlight and heat, characterizes the strong denitrification of the stratosphere, likely due to PSCs sedimentation at lower levels where the IASI sensitivity is low. For each year over the IASI period, the use of the second derivative of the HNO_3 column versus time was then found particularly valuable to detect the onset of the HNO_3 condensation to PSCs. It is captured, on average from IASI, a few days before June with a delay of 4–23 days after the maximum in total HNO_3. The corresponding temperatures ('drop temperatures') were detected between 189.2 K and 202.8 K (194.2 ± 3.8 on average over the 10 years), which demonstrated the good consistency between the 50 hPa drop temperature and the PSCs formation temperatures in that altitude region. Finally, the annual and spatial variability (within 1°× 1°) in the drop temperature was further explored from IASI total HNO_3. Inside the isocontours of 195 K for the average temperatures and of -10×10^{-5} $K.m^2.kg^{-1}.s^{-1}$ for the averaged PV at 50 hPa, the drop temperatures are detected between ~mid-May and mid-July, typically range between ~187 K to ~195 K and are associated with the highest minima (lower than -0.5×10^{14} $molec.cm^{-2}.d^{-2}$) in the second derivative of the HNO_3 total column with respect to time, indicating a strong and rapid HNO_3 depletion. Except for extreme drop temperatures (~210 K) that were found from year to year above eastern Antarctica and suspected to result from unfiltered poor quality retrievals in case of emissivity issues above ice, the range of drop temperatures is interestingly found in line with the PSCs nucleation temperature that is known, from previous studies, to strongly depend on a series a factors (e.g. meteorological conditions, HNO_3 vapour pressure, temperature threshold exposure, presence of meteoritic dust). At the edge of the vortex, considering the isocontours of 195 K for the minimum temperatures or of -10×10^{-5} $K.m^2.kg^{-1}.s^{-1}$ for the minimum PV, higher and later drop temperatures along with weakest minima in the second derivative of the HNO_3 total column with respect to time, indicating a slow HNO_3 depletion, are found. It likely results from a short temperature threshold exposure or a mixing with already depleted airmasses from the inner vortex core. The results of this study highlight the ability of IASI to measure the variations in total HNO_3 and, in particular, to capture and monitor the rapid depletion phase over the whole polar regions.

We show in this study that the IASI dataset allows capturing the variability of stratospheric HNO_3 throughout the year (including the polar night) in the Antarctic. In that respect, it offers a new observational means to monitor the relation of HNO_3 to temperature and the related formation of PSCs. Despite the limited vertical resolution of IASI which does not allow to investigate the HNO_3 uptake by the different types of PSCs during their formation and growth along the vertical profile, the HNO_3 total column measurements from IASI constitute an important new dataset for exploring the strong polar depletion over the whole stratosphere. This is particularly relevant considering the mission continuity, which will span several decades with the planned follow-on missions. Indeed, thanks to the three successive instruments (IASI-A launched in 2006 and still operating, IASI-B in 2012, and IASI-C in 2018) that demonstrate an excellent stability of the Level-1 radiances, the measurements will soon provide an unprecedented long-term dataset of HNO_3 total columns. Further work could also make use of this unique data set to investigate the relation between HNO_3, O_3, and meteorology in the changing climate.

Data availability

The IASI HNO_3 data processed with FORLI-HNO_3 v0151001 are available upon request to the corresponding author.

Author contributions

G.R. performed the analysis, wrote the manuscript and prepared the figures. C.W. and L.C. contributed to the analysis. C.W., S.S., P.-F. C. and L.C. contributed to the interpretation of the results. D.H. was responsible for the retrieval algorithm development and the processing of the IASI HNO_3 dataset. All authors contributed to the writing of the text and reviewed the manuscript.

Competing interests

The authors declare no competing interests.

Acknowledgements

IASI has been developed and built under the responsibility of the Centre National d’Etudes Spatiales (CNES, France). It is flown on board the Metop satellites as part of the EUMETSAT Polar System. The IASI L1 data are received through the EUMETCast near-real-time data distribution service. The research was funded by the F.R.S.-FNRS, the Belgian State Federal Office for Scientific, Technical and Cultural Affairs (Prodex arrangement 4000111403 IASI.FLOW) and EUMETSAT through the Satellite Application Facility on Atmospheric Composition Monitoring (ACSAF). G. Ronsmans is grateful to the Fonds pour la Formation à la Recherche dans l’Industrie et dans l’Agriculture of Belgium for a PhD grant (Boursier FRIA). L. Clarisse is a research associate supported by the F.R.S.-FNRS. C. Clerbaux is grateful to CNES for financial support. S. Solomon is supported by the National Science Foundation (NSF-1539972).

Figure captions

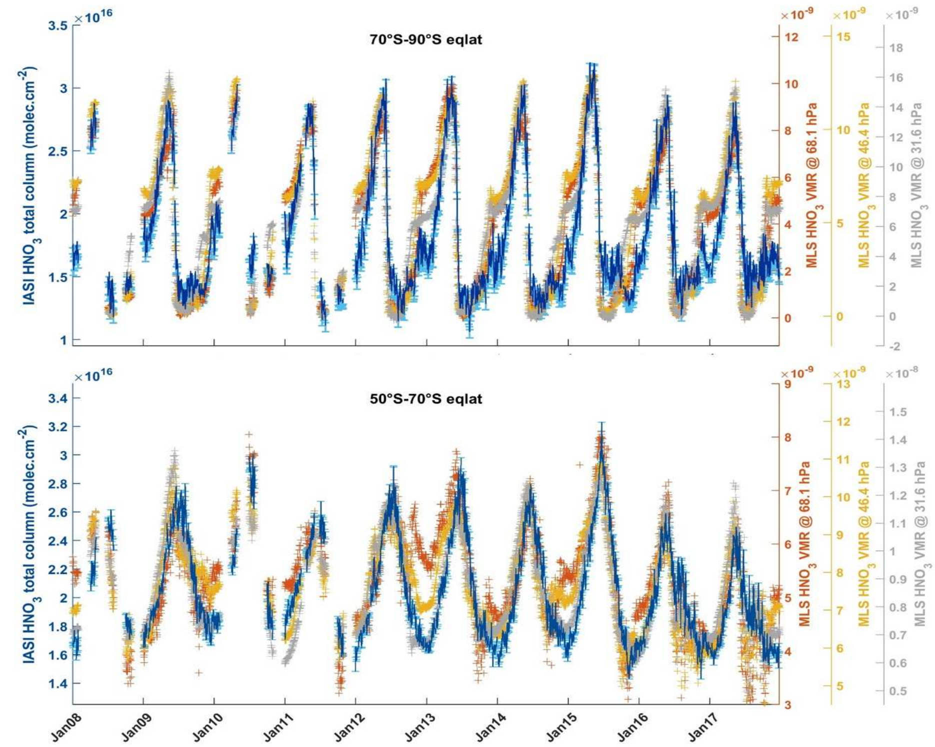

Figure 1. Time series of daily IASI total HNO_3 column (blue, left y-axis) co-located with MLS and of MLS VMR HNO_3 within 2.5×2.5 grid boxes at three pressure levels (at 30, 50 and 70 hPa; right y-axis), averaged in the 70°S–90°S (top panel) and in the 50°S–70°S (bottom panel) equivalent latitude bands. The error bars (light blue) represents 3σ, where σ is the standard deviation around the IASI HNO_3 daily average.

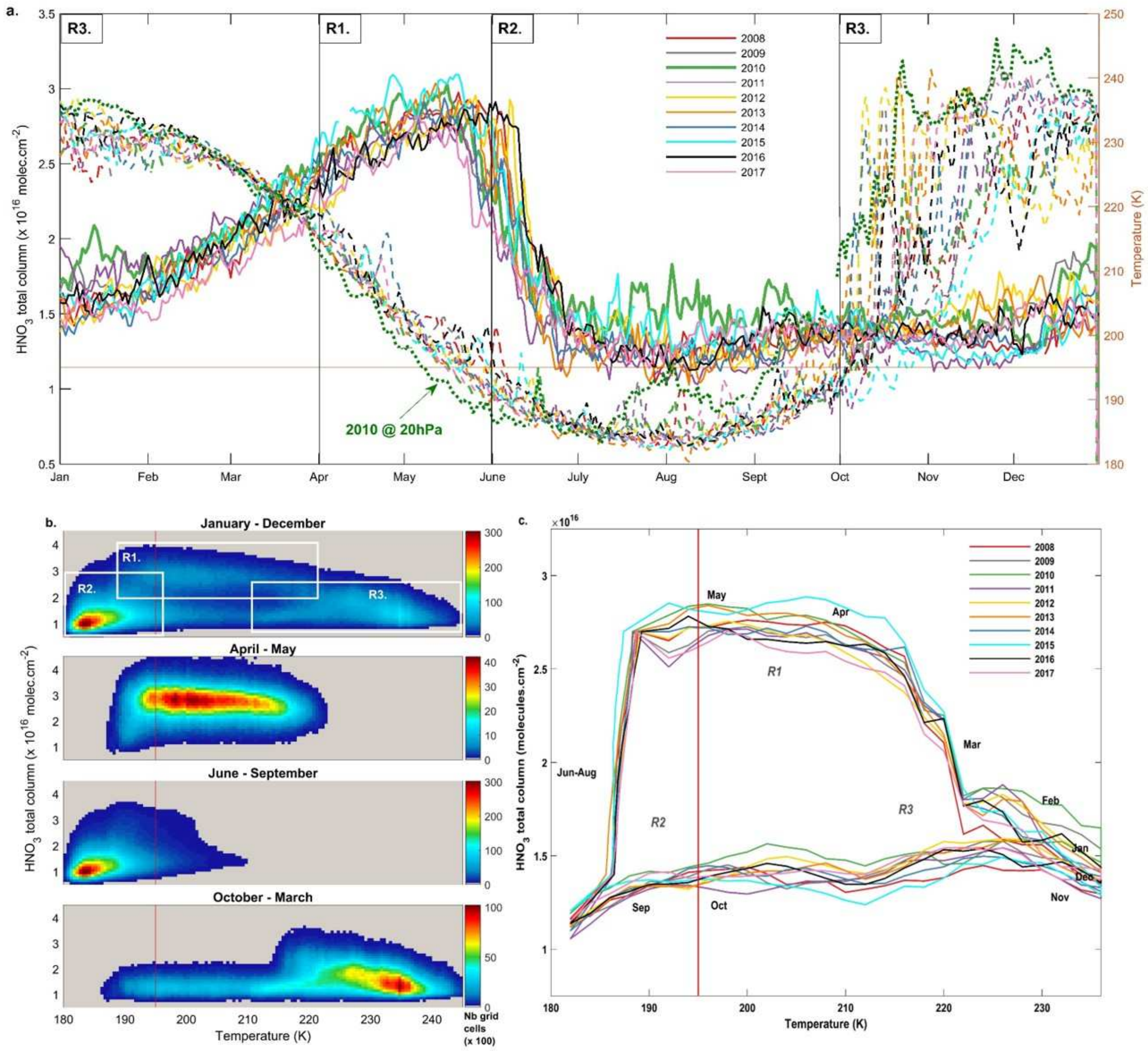

Figure 2. (a) Time series of daily averaged HNO_3 total columns (solid lines) and temperatures taken at 50 hPa (dashed lines) in the 70° - 90° S equivalent latitude band, for the years 2008 – 2017. The green dotted line represents the temperatures at 20 hPa for the year 2010. (b) HNO_3 total columns versus temperatures (at 50 hPa) histogram for the whole year (top) and for the 3 defined regimes (R1 - R3) separated in (a) for the year 2011. The colors refer to the number of gridded measurements in each cell. (c) Evolution of daily averaged HNO_3 total columns with the highest occurrence (in bins of 0.1×10^{16} molec.cm^{-2} and 2 K) as a function of the 50 hPa temperature for the years 2008 – 2017. The red horizontal or vertical lines represent the 195 K threshold temperature.

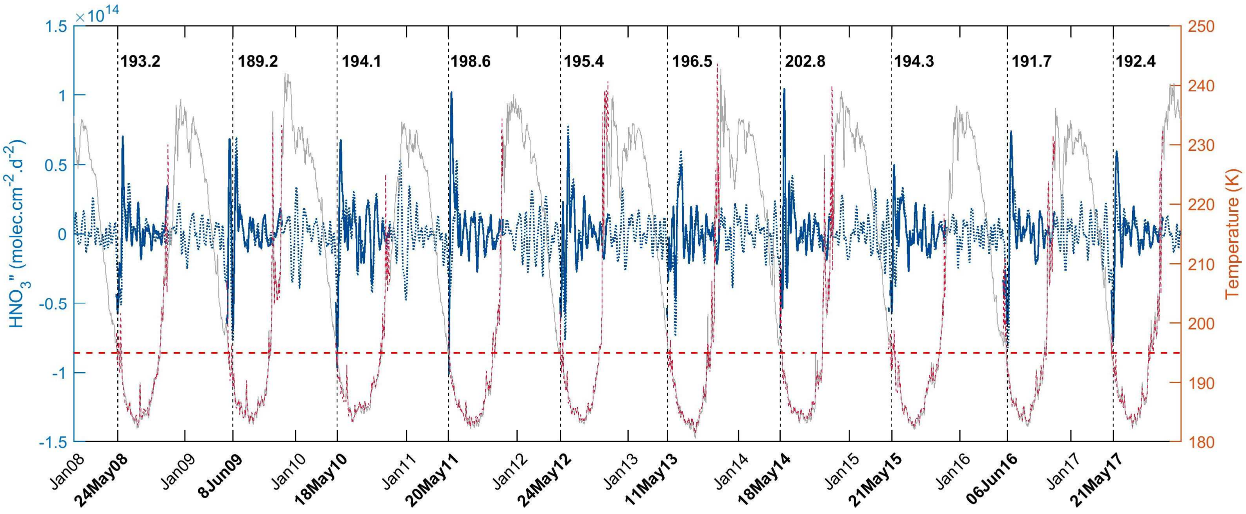

Figure 3. Time series of total HNO_3 second derivative (blue, left y-axis) and of the temperature (red, right y-axis), in the region of potential vorticity at 530 K lower than -10×10^{-5} $K.m^2.kg^{-1}.s^{-1}$. The red horizontal line corresponds to the 195 K temperature. The vertical dashed lines indicate the second derivative minimum in HNO_3 for each year. The corresponding dates (in bold, on the x-axis) and temperatures are also indicated. The time series of total HNO_3 second derivative (dashed blue) and of temperature (grey) in the 70° – 90° S Eqlat band are also represented.

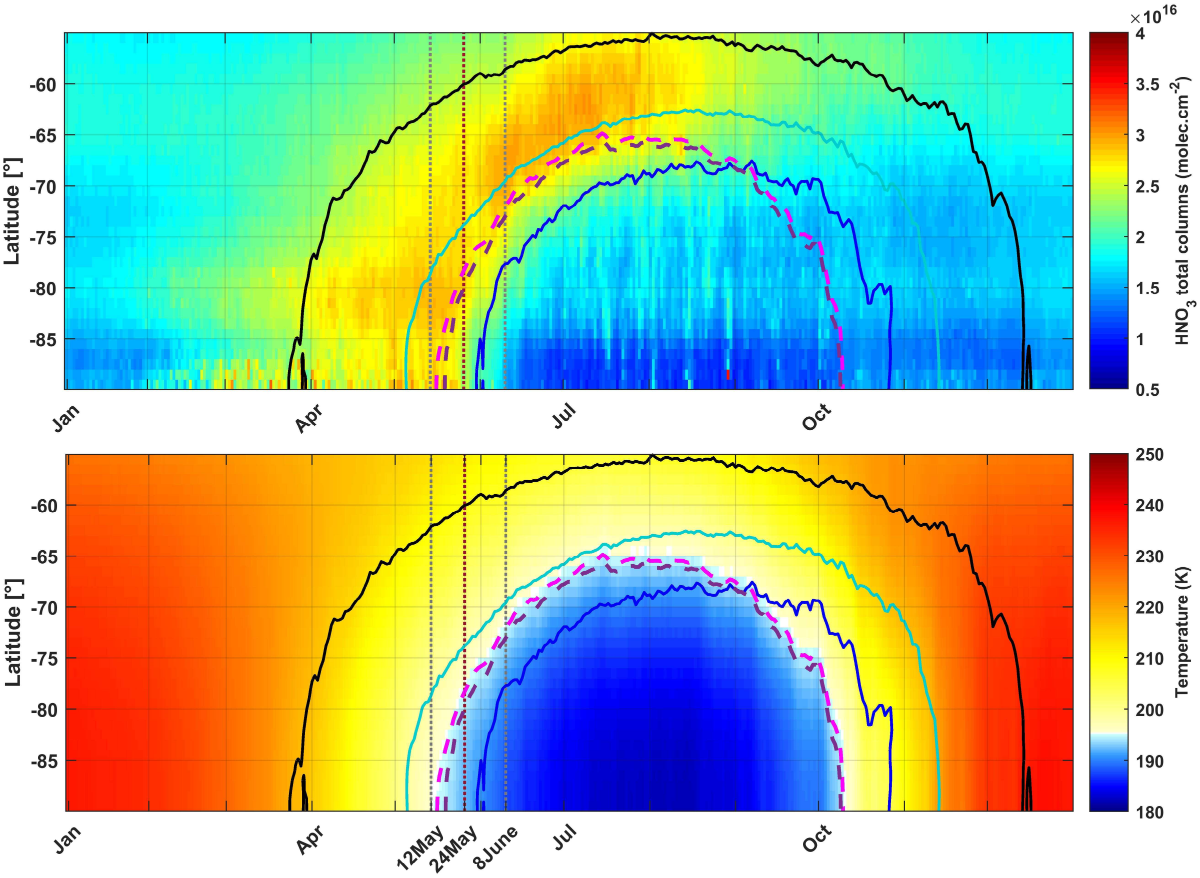

Figure 4. Zonal distributions of (a) HNO_3 total columns (in molec.cm^{-2}) from IASI and (b) temperatures at 50 hPa from ERA Interim (in K) between 55° to 90° south and averaged over the years 2008 – 2017. Three isocontours for PV of -5 (black), -8 (cyan) and -10 (blue) ($\times 10^{-5}$ K.m^2.kg^{-1}.s^{-1}) at 530 K, the isocontours for the 195 K temperature (pink) and for the averaged 194.2 K drop temperature (purple) at 50 hPa are superimposed. The vertical grey dashed lines encompass the period of the second derivative minima and the red one indicates the average date for the drop temperatures calculated in the area delimited by a -10×10^{-5} K.m^2.kg^{-1}.s^{-1} PV contour.

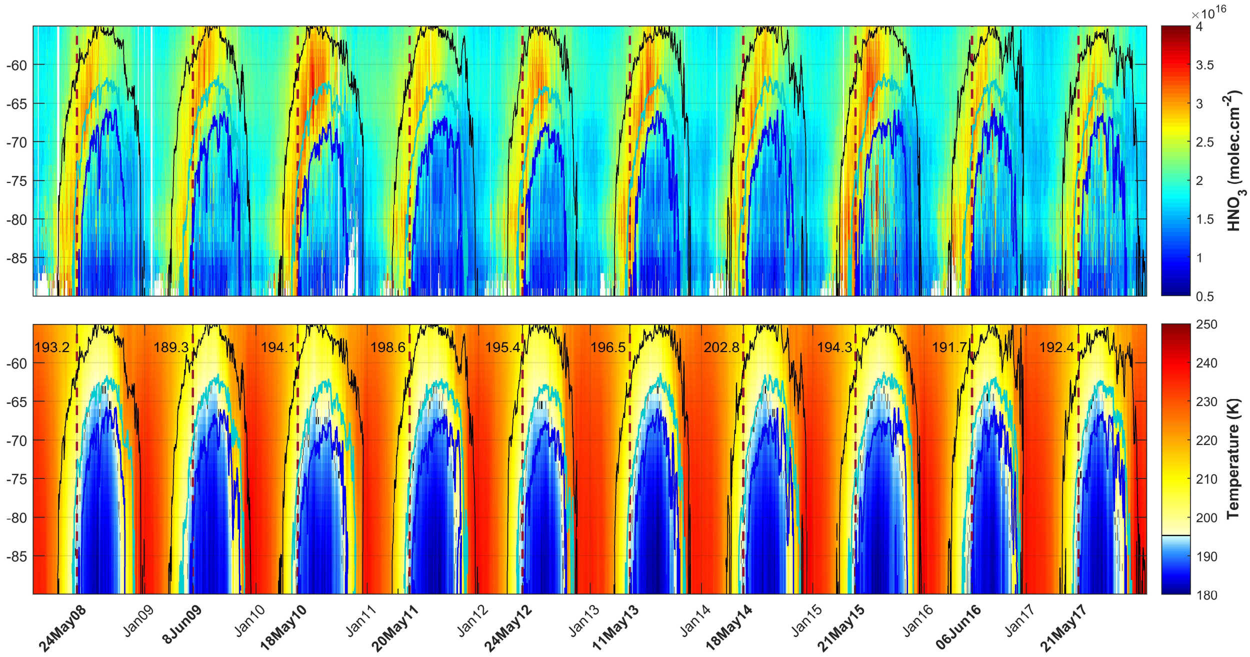

Figure 5. Zonally averaged distributions of (top) HNO_3 total columns (in molec.cm^{-2}) from IASI and (bottom) temperatures at 50 hPa from ERA Interim (in K). The latitude range is from 55° to 90° south and the isocontours are PVs of -5 (black), -8 (cyan) and -10 (blue) (× 10^{-5} K.m^2.kg^{-1}.s^{-1} at 530 K). The vertical red dashed lines correspond to the second derivative minima each year in the area delimited by a -10×10^{-5} K.m^2.kg^{-1}.s^{-1} PV contour.

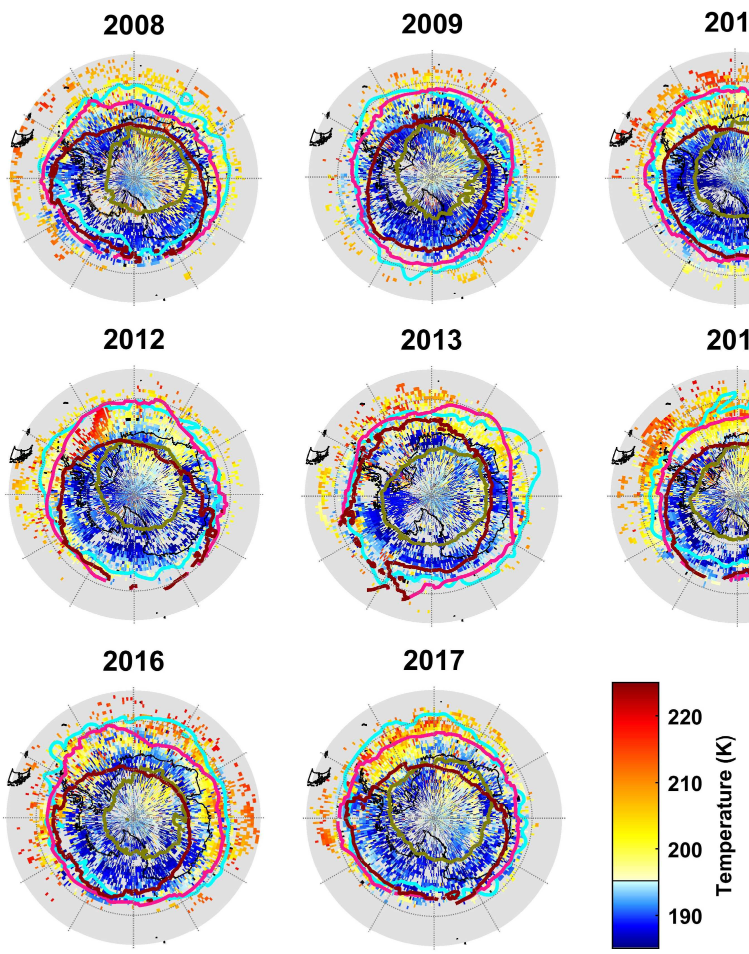

Figure 6. Spatial distribution (1°×1°) of the drop temperature at 50 hPa (K) (calculated from the total HNO_3 second derivative minima) for each year of IASI (2008–2017), in a region defined by a PV of -8×10^{-5} $K.m^2.kg^{-1}.s^{-1}$. The isocontours of -10×10^{-5} $K.m^2.kg^{-1}.s^{-1}$ at 530 K for the averaged PV (in green) and the minimum PV (in cyan) encountered over the period 10 May –15 June for each year and the isocontours of 195 K at 50 hPa for the averaged (in red) and the minimum (in pink) temperatures over the same period are represented.

References

Braun, M., Grooß, J.-U., Woiwode, W., Johansson, S., Höpfner, M., Friedl-Vallon, F., Oelhaf, H., Preusse, P., Ungermann, J., Sinnhuber, B.-M., Ziereis, H., and Braesicke, P.: Nitrification of the lowermost stratosphere during the exceptionally cold Arctic winter 2015/16, Atmospheric Chemistry and Physics Discussions, https://doi.org/10.5194/acp-2019-108, 2019.

Carslaw, K. S., Luo, B. P., and Peter, T.: An analytical expression for the composition of aqueous {HNO_3-H_2SO_4-H_2O} stratospheric aerosols including gas phase removal of HNO_3, Geophys. Res. Lett., 22, 1877–1880, https://doi.org/10.1029/95GL01668, 1995.

Carslaw, K. S., Wirth, M., Tsias, A., Luo, B. P., Dörnbrack, A., Leutbecher, M., Volkert, H., Renger, W., Bacmeister, J. T., Reimer, E., and Peter, T.: Increased stratospheric ozone depletion due to mountain-induced atmospheric waves, Nature, 391, 675–678, https://doi.org/10.1038/35589, 1998.

Clerbaux, C., Boynard, A., Clarisse, L., George, M., Hadji-Lazaro, J., Herbin, H., Hurtmans, D., Pommier, M., Razavi, A., Turquety, S., Wespes, C., and Coheur, P.-F.: Monitoring of atmospheric composition using the thermal infrared IASI/MetOp sounder, Atmospheric Chemistry and Physics, 9, 6041–6054, https://doi.org/10.5194/acp-9-6041-2009, 2009.

de Laat, A. T. J. and van Weele, M.: The 2010 Antarctic ozone hole: Observed reduction in ozone destruction by minor sudden stratospheric warmings, Scientific Reports, 1, 38, https://doi.org/10.1038/srep00038, 2011.

de Zafra, R. and Smyshlyaev, S. P.: On the formation of HNO3 in the Antarctic mid to upper stratosphere in winter, Journal of Geophysical Research, 106, 23 115, https://doi.org/10.1029/2000JD000314, 2001.

Grooß, J. U., Engel, I., Borrmann, S., Frey, W., Günther, G., Hoyle, C. R., Kivi, R., Luo, B. P., Molleker, S., Peter, T., Pitts, M. C., Schlager, H., Stiller, G., Vömel, H., Walker, K. a., and Müller, R.: Nitric acid trihydrate nucleation and denitrification in the Arctic stratosphere, Atmospheric Chemistry and Physics, 14, 1055–1073, https://doi.org/10.5194/acp-14-1055-2014, 2014.

Hanson, D. and Mauersberger, K.: Laboratory studies of the nitric acid trihydrate: Implications for the south polar stratosphere, Geophysical Research Letters, 15, 855–858, https://doi.org/10.1029/GL015i008p00855, 1988.

Harris, N. R. P., Lehmann, R., Rex, M., and von der Gathen, P.: A closer look at Arctic ozone loss and polar stratospheric clouds, Atmospheric Chemistry and Physics, 10, 8499–8510, https://doi.org/10.5194/acp-10-8499-2010, 2010.

Hilton, F., Armante, R., August, T., Barnet, C., Bouchard, A., Camy-Peyret, C., Capelle, V., Clarisse, L., Clerbaux, C., Coheur, P.-F., Collard, A., Crevoisier, C., Dufour, G., Edwards, D., Faijan, F., Fourrié, N., Gambacorta, A., Goldberg, M., Guidard, V., Hurtmans, D., Illingworth, S., Jacquinet-Husson, N., Kerzenmacher, T., Klaes, D., Lavanant, L., Masiello, G., Matricardi, M., McNally, A., Newman, S., Pavelin, E., Payan, S., Péquignot, E., Peyridieu, S., Phulpin, T., Remedios, J., Schlüssel, P., Serio, C., Strow, L., Stubenrauch, C., Taylor, J., Tobin, D., Wolf, W., and Zhou, D.: Hyperspectral Earth Observation from IASI: Five Years of Accomplishments, Bulletin of the American Meteorological Society, 93, 347–370, https://doi.org/10.1175/BAMS-D-11-00027.1, 2012.

Hoffmann, L., Spang, R., Orr, A., Alexander, M. J., Holt, L. A., and Stein, O.: A decadal satellite record of gravity wave activity in the lower stratosphere to study polar stratospheric cloud formation, Atmospheric Chemistry and Physics, 17, 2901–2920, https://doi.org/10.5194/acp-17-2901-2017, 2017.

Höpfner, M., Luo, B. P., Massoli, P., Cairo, F., Spang, R., Snels, M., Di Donfrancesco, G., Stiller, G., von Clarmann, T., Fischer, H., and Biermann, U.: Spectroscopic evidence for NAT, STS, and ice in MIPAS infrared limb emission measurements of polar stratospheric clouds, Atmospheric Chemistry and Physics, 6, 1201–1219, https://doi.org/10.5194/acp-6-1201-2006, 2006.

Höpfner, M., Pitts, M. C., and Poole, L. R.: Comparison between CALIPSO and MIPAS observations of polar stratospheric clouds, Journal of Geophysical Research Atmospheres, 114, 1–15, https://doi.org/10.1029/2009JDO12114, 2009.

Hoyle, C. R., Engel, I., Luo, B. P., Pitts, M. C., Poole, L. R., Grooß, J. U., and Peter, T.: Heterogeneous formation of polar stratospheric clouds- Part 1: Nucleation of nitric acid trihydrate (NAT), Atmospheric Chemistry and Physics, 13, 9577–9595, https://doi.org/10.5194/acp-13- 9577-2013, 2013.

Hurtmans, D., Coheur, P.-F., Wespes, C., Clarisse, L., Scharf, O., Clerbaux, C., Hadji-Lazaro, J., George, M., and Turquety, S.: FORLI radiative transfer and retrieval code for IASI, Journal of Quantitative Spectroscopy and Radiative Transfer, 113, 1391–1408, https://doi.org/10.1016/j.jqsrt.2012.02.036, 2012.

James, A. D., Brooke, J. S. A., Mangan, T. P., Whale, T. F., Plane, J. M. C., and Murray, B. J.: Nucleation of nitric acid hydrates in polar stratospheric clouds by meteoric material, Atmospheric Chemistry and Physics, 18, 4519–4531, https://doi.org/10.5194/acp-18-4519- 2018, 2018.

Keys, J. G., Johnston, P. V., Blatherwick, R. D., and Murcray, F. J.: Evidence for heterogeneous reactions in the Antarctic autumn stratosphere, Nature, 361, 49–51, https://doi.org/10.1038/361049a0, 1993.

Klekociuk, A., Tully, M., Alexander, S., Dargaville, R., Deschamps, L., Fraser, P., Gies, H., Henderson, S., Javorniczky, J., Krummel, P., Petelina, S., Shanklin, J., Siddaway, J., and Stone, K.: The Antarctic ozone hole during 2010, Australian Meteorological and Oceanographic Journal, 61, 253–267, https://doi.org/10.22499/2.6104.006, 2011.

Koop, T., Luo, B., Tsias, A., and Peter, T.: Water activity as the determinant for homogeneous ice nucleation in aqueous solutions, Nature, 406, 611–614, https://doi.org/10.1038/35020537, 2000.

Kvissel, O.-K., Orsolini, Y. J., Stordal, F., Isaksen, I. S. A., and Santee, M. L.: Formation of stratospheric nitric acid by a hydrated ion cluster reaction: Implications for the effect of energetic particle precipitation on the middle atmosphere, Journal of Geophysical Research: Atmospheres, 117, n/a–n/a, https://doi.org/10.1029/2011jd017257, 2012.

Lambert, A. and Santee, M. L.: Accuracy and precision of polar lower stratospheric temperatures from reanalyses evaluated from A-Train CALIOP andMLS, COSMIC GPS RO, and the equilibrium thermodynamics of supercooled ternary solutions and ice clouds, Atmospheric Chemistry and Physics, 18, 1945–1975, https://doi.org/10.5194/acp-18-1945-2018, 2018.

Lambert, A., Santee, M. L., Wu, D. L., and Chae, J. H.: A-train CALIOP and MLS observations of early winter Antarctic polar stratospheric clouds and nitric acid in 2008, Atmospheric Chemistry and Physics, 12, 2899–2931, https://doi.org/10.5194/acp-12-2899-2012, 2012.

Lambert, A., Santee, M. L., and Livesey, N. J.: Interannual variations of early winter Antarctic polar stratospheric cloud formation and nitric acid observed by CALIOP and MLS, Atmospheric Chemistry and Physics, 16, 15 219–15 246, https://doi.org/10.5194/acp-16-15219-2016, 2016.

Lawrence, Z. D., Manney, G. L., and Wargan, K.: Reanalysis intercomparisons of stratospheric polar processing diagnostics, Atmospheric Chemistry and Physics, 18, 13 547–13 579, https://doi.org/10.5194/acp-18-13547-2018, 2018.

Lowe, D. and MacKenzie, A. R.: Polar stratospheric cloud microphysics and chemistry, Journal of Atmospheric and Solar-Terrestrial Physics, 70, 13–40, https://doi.org/10.1016/j.jastp.2007.09.011, 2008.

Molleker, S., Borrmann, S., Schlager, H., Luo, B., Frey, W., Klingebiel, M., Weigel, R., Ebert, M., Mitev, V., Matthey, R., Woiwode, W., Oelhaf, H., Dörnbrack, A., Stratmann, G., Grooß, J.-U., Günther, G., Vogel, B., Müller, R., Krämer, M., Meyer, J., and Cairo, F.: Microphysical properties of synoptic-scale polar stratospheric clouds: in situ measurements of unexpectedly large HNO3-containing particles in the Arctic vortex, Atmospheric Chemistry and Physics, 14, 10 785–10 801, https://doi.org/10.5194/acp-14-10785-2014, 2014.

Murphy, D. M. and Koop, T.: Review of the vapour pressures of ice and supercooled water for atmospheric applications, Quarterly Journal of the Royal Meteorological Society, 131, 1539–1565, https://doi.org/10.1256/qj.04.94, 2005.

Peter, T.: Microphysics and heterogeneous chemistry of polar stratospheric clouds, Annual Review of Physical Chemistry, 48, 785–822, https://doi.org/10.1146/annurev.physchem.48.1.785, 1997.

Peter, T. and Grooß, J.-U.: Chapter 4. Polar Stratospheric Clouds and Sulfate Aerosol Particles: Microphysics, Denitrification and Heterogeneous Chemistry, in: Stratospheric Ozone Depletion and Climate Change, pp. 108–144, Royal Society of Chemistry, https://doi.org/10.1039/9781849733182-00108, 2012.

Piccolo, C. and Dudhia, A.: Precision validation of MIPAS-Envisat products, Atmospheric Chemistry and Physics, 7, 1915–1923, https://doi.org/10.5194/acp-7-1915-2007, 2007.

Pitts, M. C., Poole, L. R., Dörnbrack, A., and Thomason, L. W.: The 2009-2010 Arctic polar stratospheric cloud season: A CALIPSO perspective, Atmospheric Chemistry and Physics, 11, 2161–2177, https://doi.org/10.5194/acp-11-2161-2011, 2011.

Pitts, M. C., Poole, L. R., Lambert, A., and Thomason, L.W.: An assessment of CALIOP polar stratospheric cloud composition classification, Atmospheric Chemistry and Physics, 13, 2975–2988, https://doi.org/10.5194/acp-13-2975-2013, 2013.

Pitts, M. C., Poole, L. R., and Gonzalez, R.: Polar stratospheric cloud climatology based on CALIPSO spaceborne lidar measurements from 2006 to 2017, Atmospheric Chemistry and Physics, 18, 10 881–10 913, https://doi.org/10.5194/acp-18-10881-2018, 2018.

Rodgers, C. D.: Inverse Methods for Atmospheric Sounding - Theory and Practice, vol. 2 of Series on Atmospheric Oceanic and Planetary Physics, World Scientific Publishing Co. Pte. Ltd., https://doi.org/10.1142/9789812813718, 2000.

Ronsmans, G., Langerock, B., Wespes, C., Hannigan, J. W., Hase, F., Kerzenmacher, T., Mahieu, E., Schneider, M., Smale, D., Hurtmans, D., De Mazière, M., Clerbaux, C., and Coheur, P.-F.: First characterization and validation of FORLI-HNO3 vertical profiles retrieved from IASI/Metop, Atmospheric Measurement Techniques, 9, 4783–4801, https://doi.org/10.5194/amt-9-4783-2016, 2016.

Ronsmans, G.,Wespes, C., Hurtmans, D., Clerbaux, C., and Coheur, P.-F.: Spatio-temporal variations of nitric acid total columns from 9 years of IASI measurements – a driver study, Atmospheric Chemistry and Physics, 18, 4403–4423, https://doi.org/10.5194/acp-18-4403-2018, 2018.

Santee, M. L., Manney, G. L., Froidevaux, L., Read, W. G., and Waters, J. W.: Six years of UARS Microwave Limb Sounder HNO_3 observations : Seasonal, interhemispheric, and interannual variations in the lower stratosphere, Journal of Geophysical Research, 104, 8225–8246, https://doi.org/10.1029/1998JD100089, 1999.

Santee, M. L., Lambert, A., Read, W. G., Livesey, N. J., Cofield, R. E., Cuddy, D. T., Daffer, W. H., Drouin, B. J., Froidevaux, L., Fuller, R. A., Jarnot, R. F., Knosp, B. W., Manney, G. L., Perun, V. S., Snyder, W. V., Stek, P. C., Thurstans, R. P., Wagner, P. A., Waters, J. W., Muscari, G., de Zafra, R. L., Dibb, J. E., Fahey, D. W., Popp, P. J., Marcy, T. P., Jucks, K. W., Toon, G. C., Stachnik, R. A., Bernath, P. F., Boone, C. D., Walker, K. A., Urban, J., and Murtagh, D.: Validation of the Aura Microwave Limb Sounder HNO3 measurements, Journal of Geophysical Research, 112, 1–22, https://doi.org/10.1029/2007JD008721, 2007.

Schreiner, J., Voigt, C., Weisser, C., Kohlmann, A., Mauersberger, K., Deshler, T., Kröger, C., Rosen, J., Kjome, N., Larsen, N., Adriani, A., Cairo, F., Donfrancesco, G. D., Ovarlez, J., Ovarlez, H., and Dörnbrack, A.: Chemical , microphysical , and optical properties of polar stratospheric clouds, Journal of Geophysical Research, 108, 1–10, https://doi.org/10.1029/2001JD000825, 2003.

Schreiner, W., Rocken, C., Sokolovskiy, S., Syndergaard, S., and Hunt, D.: Estimates of the precision of GPS radio occultations from the COSMIC/FORMOSAT-3 mission, Geophysical Research Letters, 34, 1–5, https://doi.org/10.1029/2006GL027557, 2007.

Sheese, P. E., Walker, K. A., Boone, C. D., Bernath, P. F., Froidevaux, L., Funke, B., Raspollini, P., and von Clarmann, T.: ACE-FTS ozone, water vapour, nitrous oxide, nitric acid, and carbon monoxide profile comparisons with MIPAS and MLS, Journal of Quantitative Spectroscopy and Radiative Transfer, 186, 63–80, https://doi.org/10.1016/j.jqsrt.2016.06.026, 2017.

Snels, M., Scoccione, A., Liberto, L. D., Colao, F., Pitts, M., Poole, L., Deshler, T., Cairo, F., Cagnazzo, C., and Fierli, F.: Comparison of Antarctic polar stratospheric cloud observations by ground-based and space-borne lidar and relevance for chemistry–climate models, Atmospheric Chemistry and Physics, 19, 955–972, https://doi.org/10.5194/acp-19-955-2019, 2019.

Solomon, S.: Stratospheric ozone depletion: A review of concepts and history, Reviews of Geophysics, 37, 275–316, https://doi.org/10.1029/1999RG900008, 1999.

Spang, R., Hoffmann, L., Höpfner, M., Griessbach, S., Müller, R., Pitts, M. C., Orr, A. M. W., and Riese, M.: A multi-wavelength classification method for polar stratospheric cloud types using infrared limb spectra, Atmospheric Measurement Techniques, 9, 3619–3639, https://doi.org/10.5194/amt-9-3619-2016, 2016.

Spang, R., Hoffmann, L., Müller, R., Grooß, J.-U., Tritscher, I., Höpfner, M., Pitts, M., Orr, A., and Riese, M.: A climatology of polar stratospheric cloud composition between 2002 and 2012 based on MIPAS/Envisat observations, Atmospheric Chemistry and Physics, 18, 5089–5113, https://doi.org/10.5194/acp-18-5089-2018, 2018.

Toon, O. B., Hamill, P., Turco, R. P., and Pinto, J.: Condensation of HNO3 and HCl in the winter polar stratospheres, Geophysical Research Letters, 13, 1284–1287, https://doi.org/10.1029/GL013i012p01284, 1986.

Urban, J., Pommier, M., Murtagh, D. P., Santee, M. L., and Orsolini, Y. J.: Nitric acid in the stratosphere based on Odin observations from 2001 to 2009 – Part 1: A global climatology, Atmospheric Chemistry and Physics, 9, 7031–7044, https://doi.org/10.5194/acp-9-7031- 2009, 2009.

Voigt, C., Schreiner, J., Kohlmann, A., Zink, P., Mauersberger, K., Larsen, N., Deshler, T., Kro, C., Rosen, J., Adriani, A., Cairo, F., Donfrancesco, G. D., Viterbini, M., Ovarlez, J., Ovarlez, H., and David, C.: Nitric Acid Trihydrate (NAT) in Polar Stratospheric Clouds, Science, 290, 1756–1758, https://doi.org/10.1126/science.290.5497.1756, 2000.

Voigt, C., Schlager, H., Luo, B. P., Dörnbrack, A., Roiger, A., Stock, P., Curtius, J., Vössing, H., Borrmann, S., Davies, S., Konopka, P., Schiller, C., Shur, G., and Peter, T.: Nitric Acid Trihydrate (NAT) formation at low NAT supersaturation in Polar Stratospheric Clouds (PSCs), Atmospheric Chemistry and Physics, 5, 1371–1380, https://doi.org/10.5194/acp-5-1371-2005, 2005.

von König, M.: Using gas-phase nitric acid as an indicator of PSC composition, Journal of Geophysical Research, 107, https://doi.org/10.1029/2001jd001041, 2002.

Wang, D. Y., Blom, C. E., Ward, W. E., Fischer, H., Blumenstock, T., Hase, F., Keim, C., Liu, G. Y., Mikuteit, S., Oelhaf, H., Wetzel, G., Cortesi, U., Mencaraglia, F., Bianchini, G., Redaelli, G., Pirre, M., Catoire, V., Huret, N., Vigouroux, C., Mahieu, E., Demoulin, P.,Wood, S., Smale, D., Jones, N., Nakajima, H., Sugita, T., Urban, J., Murtagh, D., Boone, C. D., Bernath, P. F., Walker, K. a., Kuttippurath, J.,Toon, G., Piccolo, C., Brunswick, N., Zealand, N., Science, S., and Cedex, P.: Validation of MIPAS HNO3 operational data, Atmospheric Chemistry and Physics, 7, 4905–4934, https://doi.org/10.5194/acp-7-4905-2007, 2007.

Wang, X. and Michelangeli, D. V.: A review of polar stratospheric cloud formation, China Particuology, 4, 261–271, https://doi.org/10.1016/S1672-2515(07)60275-9, 2006.

Wegner, T., Grooß, J.-U., von Hobe, M., Stroh, F., Sumin´ska-Ebersoldt, O., Volk, C. M., Hösen, E., Mitev, V., Shur, G., and Müller, R.: Heterogeneous chlorine activation on stratospheric aerosols and clouds in the Arctic polar vortex, Atmospheric Chemistry and Physics, 12, 11 095–11 106, https://doi.org/10.5194/acp-12-11095-2012, 2012.

Wespes, C., Hurtmans, D., Clerbaux, C., and Coheur, P.-F.: O_3 variability in the troposphere as observed by IASI over 2008-2016: Contribution of atmospheric chemistry and dynamics, Journal of Geophysical Research: Atmospheres, 122, 2429–2451, https://doi.org/10.1002/2016JD025875, http://doi.wiley.com/10.1002/2016JD025875, 2017.

WMO: Scientific Assessment of Ozone Depletion: 2014, Global Ozone Research and Monitoring Project – Report No. 55, World Meteorological Organization, Geneva, Switzerland, 2014.

Zhu, Y., Toon, O. B., Lambert, A., Kinnison, D. E., Brakebusch, M., Bardeen, C. G., Mills, M. J., and English, J. M.: Development of a Polar Stratospheric Cloud Model within the Community Earth System Model using constraints on Type I PSCs from the 2010-2011 Arctic winter, Journal of Advances in Modeling Earth Systems, 7, 551–585, https://doi.org/10.1002/2015ms000427, 2015.